Proceedings of the Thirty-second (2022) International Ocean and Polar Engineering Conference **www.isope.org**
Shanghai, China, June 5–10, 2022

ISBN 978-1-880653-81-4; ISSN 1098-6189

A Coupled CFD and Dynamic Mooring Model for FOWT Hydrodynamics

Wenjie Zhong[1], Nina Wang[2], Decheng Wan[1]*

[1] Computational Marine Hydrodynamics Lab (CMHL), School of Naval Architecture, Ocean and Civil Engineering, Shanghai Jiao Tong University, Shanghai, China
[2] Key Laboratory of Far-shore Wind Power Technology of Zhejiang Province, Huadong Engineering Corporation Limited, Hangzhou, China
[*]Corresponding author

ABSTRACT

The fast-growing floating offshore wind turbines (FOWTs) urge a reliable tool for coupled analyses. While most studies utilize the quasi-static mooring model, the mooring dynamics has rarely been included in the coupled computational fluid dynamics (CFD) analysis of FOWTs. In the present paper, a finite element mooring dynamics code is coupled to CFD for FOWT hydrodynamics. Free-decay tests and responses in regular waves of the DeepCwind semi-submersible platform moored by catenary cables are simulated for validation purpose. Results show that the coupled model is accurate against the experiment data and exhibits greater reliability than the model-based approach.

KEY WORDS: Floating offshore wind turbines; Computational fluid dynamics; Dynamic mooring model; Coupled simulation; Free-decay test; Regular wave.

INTRODUCTION

The development of floating offshore wind turbines (FOWTs) along with the exploration of offshore wind energy has been ocean engineering trends for decades due to the demands for clean and renewable energies. FOWTs operate in deep waters where more stable wind resources abound in comparison to onshore and nearshore sites, and have become one of the research focuses among the wind energy community. As the FOWT is a multi-body system containing the wind turbine, the control sector, the tower, the floating platform and the mooring system, challenges are directly faced when trying to assess the coupling effects among the components (Liu et al., 2016). In specific, the moving platform adds six degrees of freedom (DOFs) to the mounted wind turbine, causing greater uncertainties in its aerodynamics and power production (Liu et al., 2019; Tran and Kim, 2016a). On the contrary, the hydrodynamics of the floating platform is modified due to the wind-induced constant inclination and variational pitching motion (Antonutti et al., 2016). The restoration by dynamic mooring systems is significant when the floating structure encounters severe sea conditions (Hall et al., 2014).

Methods for conducting coupled simulations of FOWTs generally fall into two classes. One is based on engineering models and the other is based on the computational fluid dynamics (CFD). The model-based method uses empirical formula for the aerodynamic and hydrodynamic loads, and possesses the feature of fast computation which is suitable for the preliminary design purpose (Dai et al., 2018; Jonkman, 2009; Nygaard et al., 2016; Robertson et al., 2014). While the low-order models in aerodynamics and hydrodynamics affect the overall accuracy and range of application of the model-based approach, the structural dynamics can be directly obtained which can be used for ultimate and fatigue load evaluations (Kvittem and Moan, 2015; Luan et al., 2017). The CFD approach has long been applied in simulating FOWTs (Cheng et al., 2019; Huang et al., 2019; Liu et al., 2017; Tran and Kim, 2015, 2016b; Yan et al., 2016). As real flow is modeled in CFD, the fluid force is simply calculated by integration of pressure and viscous stress with the accuracy dependent on the fidelity of the numerical model. Particularly for the wave structure interaction problems, wave breaking, run-up and overtopping, vortex generation and shedding are inherently included in the nonlinear governing equations. It is to note that since the structural parts are modeled as boundaries in CFD, the flexibility of the structure relies on external codes for fluid-structure interaction simulations (Carrion et al., 2014; Lee et al., 2017; Liu et al., 2019).

The distinct feature of FOWTs is the floating platform which has its prototype in offshore oil and gas industry. Different from those in offshore oil and gas productions, the mass and wave loading properties of FOWT platforms are unique considering the interaction between the platform and the mooring system. To include the role of mooring lines into CFD simulations, a coupled CFD and mooring model is required. Plenty of researches have tried using the quasi-static mooring model for either coupled hydrodynamic-mooring (Lin et al., 2021; Huang et al., 2021; Tran and Kim, 2015) or coupled aerodynamic-hydrodynamic-mooring (Cheng et al., 2019; Liu et al., 2017; Liu et al., 2019; Tran and Kim, 2016b) analysis of FOWTs. The quasi-static model solves for the mooring line profile and tension using the analytical equations with the assumption that the line is in static equilibrium. The hydrodynamic and inertial forces are neglected in the model which affects the prediction of the motion response of the moored structure and the mooring loads.

A number of studies showed that the use of dynamic models is in many cases necessary for accurately predicting mooring line loads in

FOWTs analysis, which is critical for designing the mooring system and assessing the FOWT`s safety. Masciola et al. (2013) compared the response of the DeepCwind semi-submersible in coupled simulations using the quasi-static mooring model MAP and the finite element model OrcaFlex against 1:50 scale test, and found that the platform motions are influenced by mooring dynamics only in extreme sea states but the mooring dynamics are important to the mooring line tensions in all load cases. Hall et al. (2014) compared quasi-static and finite element mooring models across three classes of floating platform designs and reached similar conclusions as Masciola et al. (2013). Thus, a CFD model that incorporates mooring line dynamics is required for the thorough understanding of FOWTs` coupling behaviors. To the authors` knowledge, among the four types of dynamic mooring models, i.e., lumped mass (LM) method, finite element method (FEM), finite difference method (FDM) and multi-body dynamics (MBD) method, only the LM method has been used in the coupled CFD simulations of FOWTs (Li et al., 2019; Zhou et al., 2019). A FDM mooring dynamics model was developed by Chen et al. (2018) and has been used for the model-based analysis of FOWTs. In Antonutti et al. (2018), the open source FEM code Code_Aster was applied for the dynamic mooring modeling in the model-based FOWT analysis.

It is found on review that the FEM dynamic mooring model has been scarcely used in the coupled CFD-mooring simulations of FOWTs. In the present paper, a fully coupled CFD and dynamic mooring model for FOWT hydrodynamics is presented and validated against published experimental and numerical data. The adopted mooring solver is an in-house FEM mooring code which uses the discontinuous Galerkin (DG) method of arbitrary spatial order to simulate flexible cables with no bending and torsional stiffness (Palm et al., 2016). The DG formulation allows the solution to be discontinuous over elemental boundaries which are related by numerical fluxes and is argued to be better suited for handling shock waves (such as snap loads) than conventional discretization approaches. The DeepCwind FOWT semi-submersible is used for the present validation purpose (Coulling et al., 2013; Koo et al., 2014). The free-decay test and motion response in regular waves of the semi-submersible platform are conducted to confirm the effectiveness of the coupled CFD and mooring model. Validation results indicate that the CFD-mooring model is accurate with respect to the experiment data and shows greater reliability than the model-based analysis.

The paper is organized as follows. The section *Numerical Models* lists the mathematical models relevant for the coupled CFD simulations including the flow model, the rigid body dynamic model, the mesh motion model and the dynamic mooring model. The details of coupling the fluid flow and the mooring lines to the rigid body are contained in the descriptions of the rigid body and mooring models, respectively. The section *Physical Model* gives detailed information of the semi-submersible and the mooring system from the experiment (Coulling et al., 2013; Koo et al., 2014). The section *Computational Details* describes the numerical setup in the present study. The validation test results are presented in the section *Results and Discussion*. Finally, concluding remarks are drawn.

NUMERICAL MODELS

Flow Model

For viscous and incompressible two-phase flows, the continuity and Navier-Stokes (N-S) equations forcing the conservations of mass and momentum are applied as

$$\nabla \cdot \boldsymbol{u} = 0 \tag{1}$$

$$\frac{\partial \rho \boldsymbol{u}}{\partial t} + \nabla \cdot (\rho(\boldsymbol{u} - \boldsymbol{u}_g)\boldsymbol{u}) = -\nabla p_d - \boldsymbol{g} \cdot \boldsymbol{x} \nabla \rho + \nabla \cdot \{\mu(\nabla \boldsymbol{u} + (\nabla \boldsymbol{u})^T)\} + \sigma \kappa \nabla \alpha \tag{2}$$

where $\boldsymbol{u}$ and p are the velocity and pressure of the flow, respectively. $\boldsymbol{u}_g$ is the velocity of grid points. p_d is the dynamic pressure defined as $p_d = p - \rho \boldsymbol{g} \cdot \boldsymbol{x}$. Pressure gradient due to surface tension at the water surface is accounted for by the fourth term on the right-hand side of equation (2).

The air-water interface is captured with the volume of fluid (VOF) model. In VOF, the surface construction is realized through the volume fraction which varies between 0 and 1 depending on the percentage of water phase in the cell volume. A water cell is marked by $\alpha = 1$, an air cell is marked by $\alpha = 0$, and the air-water interface is presented where $0 < \alpha < 1$. The advection equation of the volume fraction is given as

$$\frac{\partial \alpha}{\partial t} + \nabla \cdot (\boldsymbol{u}\alpha) + \nabla \cdot [\boldsymbol{u}_r \alpha (1 - \alpha)] = 0 \tag{3}$$

where the third term on the left-hand side is an artificial compression used for sharpening the interface. $\boldsymbol{u}_r$ is the compression velocity defined as the relative velocity between water and air. In order that the compression acts in the direction perpendicular to the water surface, the compression velocity is a function of the gradient of volume fraction. With the introduction of volume fraction, the fluid properties at a cell are evaluated by weighted average, e.g., $\rho = \alpha \rho_{water} + (1 - \alpha)\rho_{air}$.

Equations (3) and (1) - (2) are solved sequentially in the numerical time stepping using the finite volume method (FVM). The FVM is implemented by integrating each term in the equations over a control volume and relating the volume integrals to the surface integrals using Gauss`s theorem. The surface and volume integrals are both treated with the mid-point integration approximation which yields second order accuracy. The convective and diffusive fluxes at cell faces are evaluated with second order upwind and central differencing schemes, respectively. The Euler scheme is used for time integration.

The multiphase solver in OpenFOAM is adopted in coupling to the dynamic mooring model. Details of the solver are referred to Zhong et al. (2020a, 2020b). The PIMPLE algorithm is used to treat the pressure-velocity coupling problem. The principal of the algorithm is as follows: within each time step, both the inner pressure correction loop (PISO loop) and outer pressure-momentum correction loop (SIMPLE loop) are executed. In the inner loop, the pressure is recalculated with the new updated flux. In the outer loop, the velocity matrix is first rebuilt with the new flux, the pressure is then corrected with the new velocity matrix and the flux is finally corrected with the new pressure. The calculations are repeated until convergence is achieved. The solutions are regarded as being converged when the residuals of the velocity and pressure are lower than 1E-06.

Rigid Body Dynamic Model

The floating platform is treated as rigid body moving with six DOFs, i.e., surge, sway, heave, roll, pitch and yaw. The listed DOFs follow the order of linear and rotational motions along or around *x*, *y* and *z* axes. The structural motion is computed via the rigid body solver in OpenFOAM that uses an explicit time step marching within PIMPLE loop. The forces and moments are obtained by integrating pressure and viscous stress over the structural surface as

$$\boldsymbol{F} = \iint_S (p\boldsymbol{n} + \boldsymbol{\tau}) dS + \boldsymbol{F}_M \tag{4}$$

$$\boldsymbol{M} = \iint_S (\boldsymbol{r}_{CS} \times (p\boldsymbol{n} + \boldsymbol{\tau})) dS + \boldsymbol{r}_{CM} \times \boldsymbol{F}_M \tag{5}$$

where $\boldsymbol{F}_M$ is the restoring force from the dynamic mooring model. $\boldsymbol{r}_{CM}$ and $\boldsymbol{r}_{CS}$ denote the distance vector of the structural mass center to the mooring attachment point and the cell surface center, respectively.

In the motion solver, the fluid forces and moments calculated with equations (4) - (5) together with the gravity force are posed onto the structure to obtain the linear and angular accelerations with Newton`s second law. Velocities and displacements of the platform are calculated with the Newmark method (Belytschko et al., 2014) as

$$\dot{\boldsymbol{d}}_{i+1} = \dot{\boldsymbol{d}}_i + \Delta t[(1-\gamma)\ddot{\boldsymbol{d}}_i + \gamma\ddot{\boldsymbol{d}}_{i+1}] \tag{6}$$

$$\boldsymbol{d}_{i+1} = \boldsymbol{d}_i + \Delta t\dot{\boldsymbol{d}}_i + \Delta t^2[(0.5-\beta)\ddot{\boldsymbol{d}}_i + \beta\ddot{\boldsymbol{d}}_{i+1}] \tag{7}$$

where the symbol $\boldsymbol{d}$ denotes the displacement vector, and single and double dots over $\boldsymbol{d}$ mean its first and second derivatives respectively. β and γ are numerical parameters specified to 0.25 and 0.5 respectively representing the implicit and unconditionally stable scheme.

Mesh Motion Model

To accommodate the moving platform in the numerical domain, the mesh adjusts with the structural motion. The adjustment realizes through grid deformation governed by the Laplace equation below.

$$\nabla\cdot(\gamma_M\nabla\boldsymbol{d}_M) = 0 \tag{8}$$

where γ_M is the variable diffusivity based on the inverse square of the distance between cell centers and moving boundaries as

$$\gamma_M = \frac{1}{r_M{}^2} \tag{9}$$

Dynamic Mooring Model

The mooring system for the FOWT is simulated with a dynamic method (Palm et al., 2016). The dynamics of flexible mooring lines is governed by a vector-valued wave equation as

$$\frac{\partial\boldsymbol{r}}{\partial t^2} = \frac{1}{\gamma_0}\frac{\partial\boldsymbol{T}}{\partial s} + \frac{\boldsymbol{f}}{\gamma_0} \tag{10}$$

where γ_0 is the line mass per meter. $\boldsymbol{r}$ denotes the mooring line position in the inertia frame and s is the curvilinear abscissa along the unstretched line. In the mooring dynamics, only the extensional stiffness is included while the bending and torsional stiffnesses are ignored, which is exact for chains and proper approximation for most mooring line materials in operation. Thus, the internal moment $\boldsymbol{M}$ is simply set to zero in the modeling, and the axial tension force vector $\boldsymbol{T}$ is always tangential to the cable as

$$\boldsymbol{T} = T(\varepsilon,\dot{\varepsilon})\frac{\boldsymbol{q}}{1+\varepsilon} \tag{11}$$

$$\boldsymbol{q} = \frac{\partial\boldsymbol{r}}{\partial s} \tag{12}$$

$$\varepsilon = |\boldsymbol{q}| - 1 \tag{13}$$

where ε is the axial strain. T is the magnitude of tension which contains the constitutive relation of the mooring line as a function of strain and strain rate. For a linear elastic cable, the tension force expresses as

$$T(\varepsilon) = EA\varepsilon \tag{14}$$

The symbol $\boldsymbol{f}$ in equation (10) represents all external forces on the mooring line as

$$\boldsymbol{f} = \boldsymbol{f}_a + \boldsymbol{f}_b + \boldsymbol{f}_c + \boldsymbol{f}_d \tag{15}$$

$\boldsymbol{f}_a$ includes the inertia force and the added mass force which exist for structures accelerating in fluids as

$$\boldsymbol{f}_a = \rho_f A(C_{Mt}\boldsymbol{a}_{r,t} + C_{Mn}\boldsymbol{a}_{r,n} + \boldsymbol{a}_f) \tag{16}$$

where C_M is the added mass coefficient, and subscripts t and n mean the tangential and normal directions respectively. $\boldsymbol{a}$ is the acceleration vector.

$\boldsymbol{f}_b$ is the net force from buoyancy written as

$$\boldsymbol{f}_b = \gamma_0\frac{\rho_c-\rho_f}{\rho_c}\boldsymbol{g} \tag{17}$$

where ρ_c and ρ_f are the material density of the mooring line and fluid, respectively.

$\boldsymbol{f}_c$ is the contact force between the mooring line and the ground. In the present study, the bilinear spring and damper model is used for the normal force to the contact plane and dynamic friction is implemented for the tangential force. For a horizontal sea floor, the contact force vector is given as

$$\boldsymbol{f}_c = \begin{cases} \boldsymbol{G}_v + \boldsymbol{G}_h & if\,(z_G - r_z) \geq 0 \\ 0 & otherwise \end{cases} \tag{18}$$

$$\boldsymbol{G}_v = (K_G d_c(z_G - r_z) - 2\xi_G\sqrt{K_G\gamma_0 d_c}\,\min(\dot{r}_z, 0))\boldsymbol{z} \tag{19}$$

$$\boldsymbol{G}_h = \mu f_{bz}\tanh\left(\frac{\pi\dot{r}_{xy}}{v_\mu}\right)\frac{\dot{\boldsymbol{r}}_{xy}}{|\dot{\boldsymbol{r}}_{xy}|} \tag{20}$$

where z_G is the vertical position of the ground. K_G and ξ_G are the stiffness and ratio of critical damping for the cable-ground interaction, respectively, and are chosen as 3.0e6 Pa/m and 1.0 respectively in the present study. μ is the friction coefficient with a user-specified velocity v_μ for the maximum friction.

$\boldsymbol{f}_d$ is the drag force proportional to the square of the relative velocity between the structure and fluid as

$$\boldsymbol{f}_d = 0.5\rho_f d\sqrt{1+\varepsilon}(C_{Dt}|\boldsymbol{v}_{r,t}|\boldsymbol{v}_{r,t} + C_{Dn}|\boldsymbol{v}_{r,n}|\boldsymbol{v}_{r,t}) \tag{21}$$

where C_D is the drag coefficient, and $\boldsymbol{v}$ is the velocity vector.

The DG method with Legendre basis functions of arbitrary order p is used to spatially discretize the dynamic equation of mooring line (Palm et al., 2013). One prominent feature of the high-order method is the exponential convergence in smooth solutions, e.g., hanging catenary, and thus sufficient accuracy can be obtained in engineering applications using only a few high order elements. The dynamic equation advances in time with the second order explicit Leap-Frog scheme. The time step size in the mooring model is restricted by the mesh size and order to maintain numerical stability. Due to the high stiffness in the mooring line, the time step size in the mooring solver is in general much smaller than that of the CFD solver.

During the coupled simulation, the mooring attachment points on the platform are used as Dirichlet boundary conditions for the mooring solver. Then the resultant force from each mooring line is returned to the CFD solver for the rigid body dynamics. Since difference in time step length exists between the coupled solvers, interpolation in time is required for imposing the boundary conditions. In the coupled model, the mooring solver is lagging a fraction ϕ of the latest time step in the CFD solver as (e.g., at the kth time step)

$$t_m^k = (1-\phi)t_f^k + \phi t_f^{k-1} \tag{22}$$

The position and velocity at the cable end point are interpolated using the latest mooring attachment point position P_k based on constant acceleration as

$$r_k(\tau) = r(0) + (v(0) + 0.5a_k\tau)\tau \tag{23}$$

$$v_k(\tau) = v(0) + a_k\tau \tag{24}$$

$$a_k = \frac{1}{0.5\Delta t_k^{\,2}}(P_k - r_k(0) - v_k(0)\Delta t_k) \tag{25}$$

where τ in [0, t_m^k- t_m^{k-1}] is the local time in the interpolation interval. Δt_k is the time interval of constant acceleration.

PHYSICAL MODEL

Semi-Submersible Platform

The DeepCwind semi-submersible platform applied in deep waters for supporting FOWTs is used in the present hydrodynamic-mooring simulations (Coulling et al., 2013; Koo et al., 2014). The platform consists of three offset columns with larger diameter base columns as heave plate components, one central column linking to the tower base, four sets of level pontoons, and three cross braces as shown in **Fig. 1**(a). Main parameters of the platform are given in **Table 1** and **Fig. 1**(b). For details of the structure see Coulling et al. (2013).

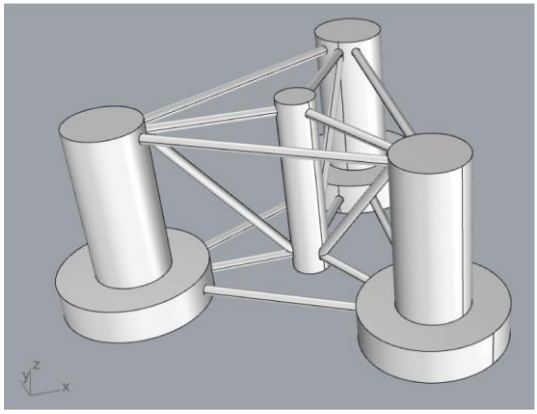

(a) 3D view

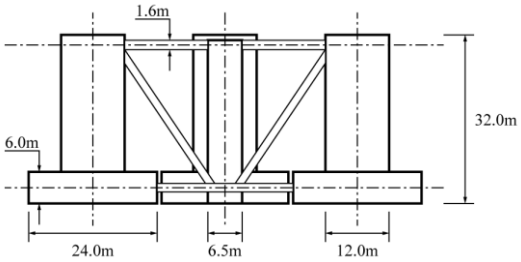

(b) Lateral view

Figure 1. Sketch of the DeepCwind semi-submersible platform.

Catenary Mooring System

A mooring system composed of three evenly distributed catenary mooring lines is used to restrain the platform motions. **Fig. 2** illustrates the arrangement of the platform and mooring system with respect to the inertia frame. The anchors of the mooring lines locate at 837.6m from the centerline of the platform with a water depth of 200m. The fairleads of the mooring lines are placed at the top of base columns, i.e., 40.868m from the centerline of the platform and 14m below the still water level. Main parameters of the mooring line are given in **Table 2**. For details of the mooring system see Coulling et al. (2013).

Table 1. Main parameters of the semi-submersible platform.

Parameters	Value
Depth of platform base below SWL	20 m
Elevation of central column above SWL	10 m
Displacement	13986.8 m^3
Center of mass location below SWL	14.4 m
Platform roll inertia about CM	8.011×10^9 kg·m^2
Platform pitch inertia about CM	8.011×10^9 kg·m^2
Platform yaw inertia about centerline	1.391×10^{10} kg·m^2

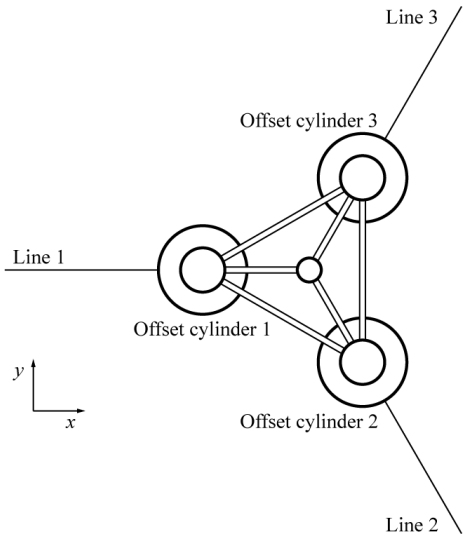

Figure 2. Arrangement of the platform and mooring system.

Table 2. Main parameters of the catenary mooring line.

Parameters	Value
Unstretched length	835.5 m
Diameter	0.0766 m
Equivalent mass density	113.35 kg/m
Equivalent axial stiffness	7.536×10^8 N
Normal drag coefficient	2.00
Tangential drag coefficient	0.40
Normal Added mass coefficient	0.80
Tangential added mass coefficient	0.25

COMPUTATIONAL DETAILS

Computational Domain and Boundary Conditions

A cuboid computational domain with dimensions of 900m (x) × 400m (y) × 300m (z) is built around the semi-submersible platform as shown in **Fig. 3**(a). The origin of the coordinate system is placed at the

intersection of the platform centerline and the still wave level with the *x* axis aligned with the wave propagation direction. The inlet and outlet locate at 300m and 600m away from the origin respectively, and are used for wave generation and active absorption respectively (Higuera et al., 2013). The structural surface and the seabed are modeled as no-slip and no-flux walls. The top boundary acts as connecting to the atmosphere permitting only outward fluxes. Front and back sides of the domain are treated as slip patch. Note that only the semi-submersible excluding the rotor, nacelle and tower is modeled while the effect of the wind turbine on the mass property has been considered.

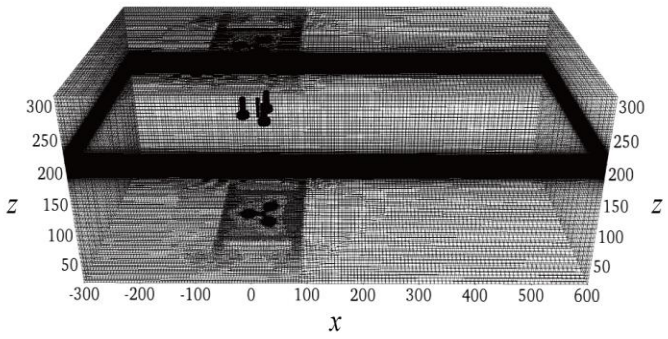

(a) Overall mesh

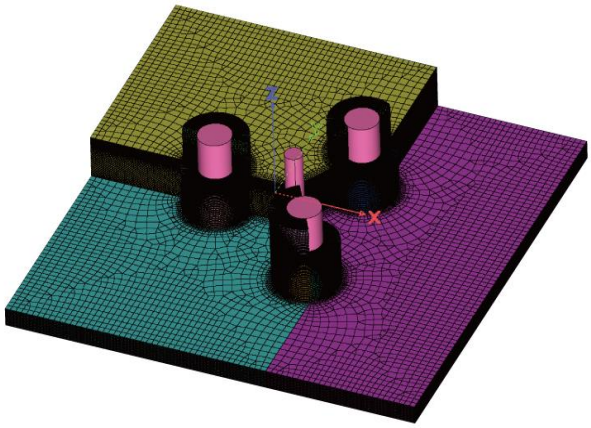

(b) Example of block mesh assembly

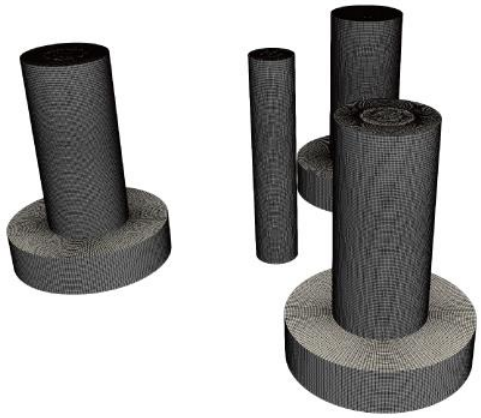

(c) Surface mesh on the platform

Figure 3. Computational domain and mesh setup.

Mesh Generation

A block structured mesh is constructed with Pointwise. Note that to simply the mesh generation, the pontoons and cross braces are not included in the modeling. Views of the overall mesh layout, the block mesh assembly and the surface mesh on the platform are shown in **Fig. 3**. As shown in the **Fig. 3**(a), grids are refined around the platform and near the free surface. The square region 150m (*x*) × 150m (*y*) covering the platform and the outside region are both filled with prism cells by extruding unstructured surface meshes (see **Fig. 3**(b)). The structural surface mesh on the offset and central columns has an average size of 0.2m (*arc*) × 0.25m (*z*), and clusters at the water surface (see **Fig. 3**(c)). The mesh sums up to 6.7 million cells. Note that an adaptive time step scheme is used for the present simulations to guarantee a maximum CFL value of 0.5.

RESULTS AND DISCUSSION

Free-Decay Test

To validate the coupled CFD-mooring model, free-decay tests of the DeepCwind platform are first conducted. The free-decay motions in three DOFs, i.e., surge, heave and pitch, are considered. In the test, the platform is released from an initial position away from the equilibrium state, which is kept the same as the experiments (Coulling et al., 2013).

The free-decay motion responses of the semi-submersible platform in surge and pitch are shown in **Fig. 4**. The predicted results are compared with the existing numerical results obtained by the potential flow model-based and CFD methods. As shown in **Fig. 4**, the present simulation results agree well with the published data though there exists small discrepancy for the surge response. It is observed that the CFD simulations predict the lowest magnitude of surge response during each free-decay circle, which is regarded as the effect of the inclusion of fluid viscosity compared to the potential flow model-based approach.

The calculated periods of the free-decay motions are compared to the experimental and numerical results in **Table 3**. It is seen that the present results obtained by the coupled CFD and dynamic mooring model exhibit a good agreement to the MARIN test data (Coulling et al., 2013). The perfect match of FAST results to the experiments is due to the tuned drag and added mass coefficients used in the hydrodynamic module HydroDyn which adopts the potential flow theory (Coulling et al., 2013). Except for the FAST results, the present model gives lower error in motion period than other numerical results (Luan et al., 2013; Tran and Kim, 2015). It is noted that a simplified semi-submersible platform with no pontoons and cross braces is used in the present simulations, which contributes to the deviations in results. Furthermore, considering the scale effect, structural flexibility of the platform, and uncertainties in the experiments, the errors in free-decay period for the present model are acceptable.

Motion Responses Under Regular Waves

The dynamic responses of the moored semi-submersible platform under regular waves are simulated with the coupled CFD and mooring model. Parameters of the waves are given in **Table 4**. Note that two amplitudes for the wave periods of 14.3s and 20.0s are considered for the purpose of assessing the nonlinearity in the motion response. The response amplitude operator (RAO) defined as the response amplitude of a field variable per amplitude of the regular wave is used to evaluate the platform hydrodynamics. Only surge, heave and pitch responses are analyzed herein due to the symmetry of the flow field around the platform as indicated by **Fig. 2**.

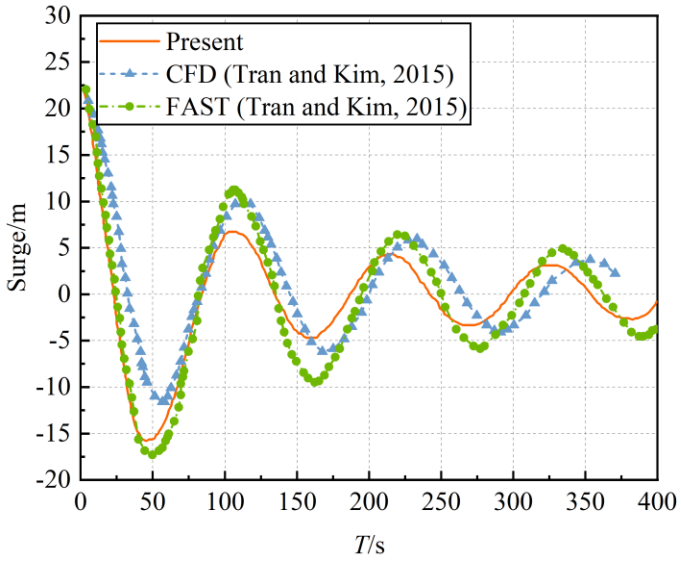

(a) Surge

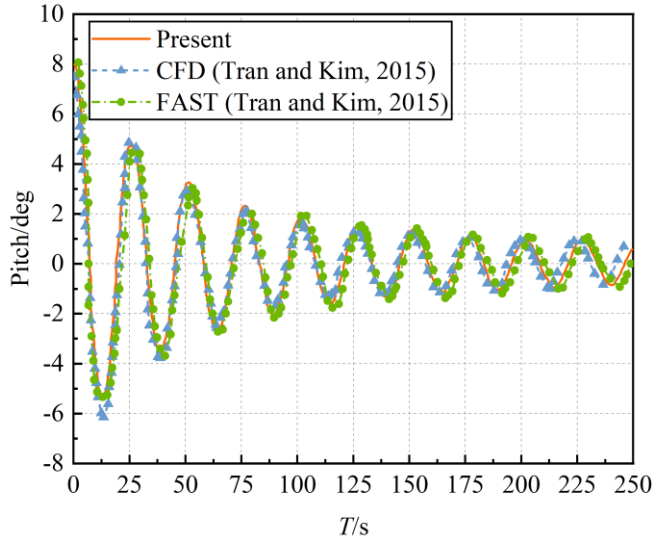

(b) Pitch

Figure 4. Comparison of free-decay motions of the platform.

Table 3. Comparison of free-decay motion periods of the platform.

Method	Surge	Heave	Pitch
Present	108.5 s	17.6 s	25.8 s
Experiment (Coulling et al., 2013)	107.0 s	17.5 s	26.8 s
FAST (Coulling et al., 2013)	107.0 s	17.3 s	26.8 s
Simo/Riflex+TDHMILL (Luan et al., 2013)	115.9 s	17.1 s	25.8 s
AQWA (Tran and Kim, 2015)	112.5 s	17.3 s	25.4 s

Table 4. Parameters of the regular waves.

Cases	Amplitude	Period	Depth
1	3.57 m	14.3 s	200 m
2	3.79 m	20.0 s	200 m
3	5.15 m	12.1 s	200 m
4	5.37 m	14.3 s	200 m
5	5.56 m	20.0 s	200 m

The RAOs in surge, heave and pitch are plotted in **Fig. 5** which compares the present results to the experimental data and FAST results from Coulling et al. (2013). Note that the label of *x*-axis in the figure is related to the case order in **Table 4**. It is seen that the RAOs obtained by the CFD-mooring model show better agreement with the experiment than FAST. The large discrepancy for FAST computation is likely due to its quadratic damping model which depends on empirical coefficients for estimating hydrodynamic loads. It is shown in **Fig. 5** that the platform motions when the wave period equal 20s are evidently larger than those at the values of 12.1s and 14.3s. It means that the hydrodynamics of the platform is more sensitive to low-frequency waves than high-frequency waves. This is consistent with the OC5 project phase II group which states that the ultimate and fatigue loads of the floating platform under wave impacts are severely underpredicted in the low-frequency region (Robertson et al., 2017). **Fig. 5** also shows that the RAOs rise with the wave amplitude at the same wave period which is in contrast to the linear theory. It implies the nonlinearity in the response of the platform associated with the fluid viscosity which is ignored in the potential flow model.

CONCLUSIONS

In this study, a coupled CFD and dynamic mooring model for the hydrodynamic predictions of FOWTs was presented. The mooring line module employs a dynamic approach with FEM discretization. Details of the models used in the coupled hydrodynamic-mooring analysis and the coupling schemes between CFD, rigid body dynamics and mooring model were described. To validate the CFD-mooring hydrodynamic model, free-decay tests and motion responses under regular waves of the DeepCwind semi-submersible platform moored by three catenary cables were simulated. Results show that the coupled model is accurate with respect to the experiment data and exhibits greater reliability than the model-based approach. In future, an extension of the present model to the coupled aerodynamic-hydrodynamic-mooring analysis will be developed for the FOWT community.

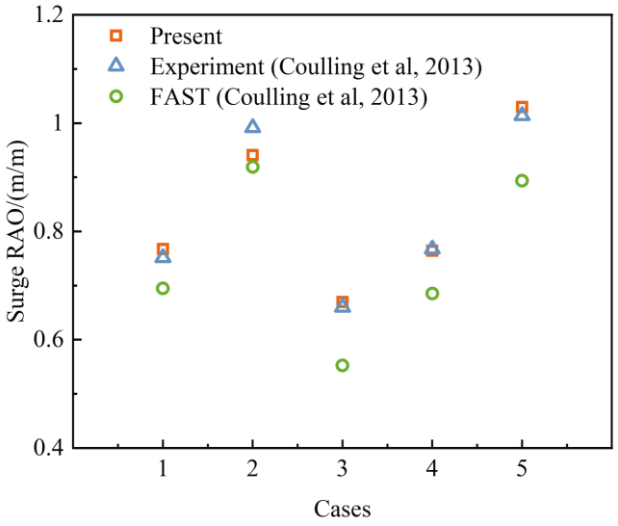

(a) Surge RAO

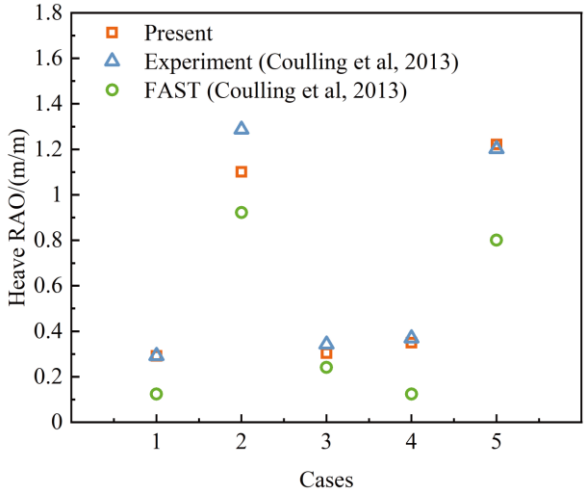

(b) Heave RAO

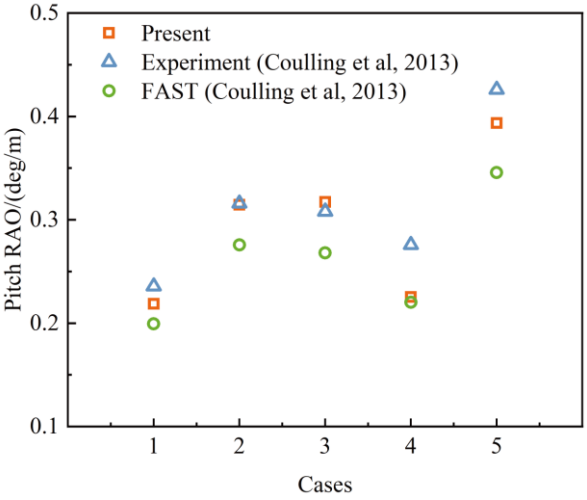

(c) Pitch RAO

Figure 5. Comparison of RAOs of the platform.

ACKNOWLEDGEMENTS

This work is supported by National Natural Science Foundation of China (52101324, 52101366, 51879159, 52131102), and the National Key Research and Development Program of China (2019YFB1704200), to which the authors are most grateful.

REFERENCES

Antonutti, R, Peyrard, C, Incecik, A, Ingram, D, and Johanning, L (2018). "Dynamic Mooring Simulation with Code_Aster with Application to a Floating Wind Turbine," *Ocean Engineering*, 151, 366-377.

Antonutti, R, Peyrard, C, Johanning, L, Incecik, A, and Ingram, D (2016). "The Effects of Wind-Induced Inclination on the Dynamics of Semi-Submersible Floating Wind Turbines in the Time Domain," *Renewable Energy*, 88, 83-94.

Belytschko, T, Liu, WK, Moran, B, and Elkhodary, K (2014). "Nonlinear finite elements for continua and structures," John wiley & sons.

Carrion, M, Steijl, R, Woodgate, M, Barakos, GN, Munduate, X, and Gomez-Iradi, S (2014). "Aeroelastic Analysis of Wind Turbines Using a Tightly Coupled CFD-CSD Method," *Journal of Fluids and Structures*, 50, 392-415.

Chen, L, Basu, B, and Nielsen, SR (2018). "A Coupled Finite Difference Mooring Dynamics Model for Floating Offshore Wind Turbine Analysis," *Ocean Engineering*, 162, 304-315.

Cheng, P, Huang, Y, and Wan, D (2019). "A Numerical Model for Fully Coupled Aero-Hydrodynamic Analysis of Floating Offshore Wind Turbine," *Ocean Engineering*, 173, 183-196.

Coulling, AJ, Goupee, AJ, Robertson, AN, Jonkman, JM, and Dagher, HJ (2013). "Validation of a FAST Semi-Submersible Floating Wind Turbine Numerical Model with DeepCwind Test Data," *Journal of Renewable and Sustainable Energy*, 5(2), 023116.

Dai, J, Hu, W, Yang, X, and Yang, S (2018). "Modeling and Investigation of Load and Motion Characteristics of Offshore Floating Wind Turbines," *Ocean Engineering*, 159, 187-200.

Hall, M, Buckham, B, and Crawford, C (2014). "Evaluating the Importance of Mooring Line Model Fidelity in Floating Offshore Wind Turbine Simulations," *Wind Energy*, 17(12), 1835-1853.

Higuera, P, Lara, JL, and Losada, IJ (2013). "Realistic Wave Generation and Active Wave Absorption for Navier-Stokes Models: Application to OpenFOAM®," *Coastal Engineering*, 71, 102-118.

Huang, Y, Cheng, P, and Wan, D (2019). "Numerical Analysis of a Floating Offshore Wind Turbine by Coupled Aero-Hydrodynamic Simulation," *Journal of Marine Science and Application*, 18(1), 82-92.

Huang, Y, Zhuang, Y, and Wan, D (2021). "Hydrodynamic Study and Performance Analysis of the OC4-DeepCWind Platform by CFD Method," *International Journal of Computational Methods*, 18(04), 2050020.

Jonkman, JM (2009). "Dynamics of Offshore Floating Wind Turbines-Model Development and Verification," *Wind Energy*: *An International Journal for Progress and Applications in Wind Power Conversion Technology*, 12(5), 459-492.

Kvittem, MI, and Moan, T (2015). "Time Domain Analysis Procedures for Fatigue Assessment of a Semi-Submersible Wind Turbine," *Marine Structures*, 40, 38-59.

Lee, K, Huque, Z, Kommalapati, R, and Han, SE (2017). "Fluid-Structure Interaction Analysis of NREL Phase VI Wind Turbine: Aerodynamic Force Evaluation and Structural Analysis Using FSI Analysis," *Renewable Energy*, 113, 512-531.

Li, L, Liu, Y, Yuan, Z, and Gao, Y (2019). "Dynamic and Structural

Performances of Offshore Floating Wind Turbines in Turbulent Wind Flow," *Ocean Engineering*, 179, 92-103.

Lin, Z, Qian, L, and Bai, W (2021). "A Coupled Overset CFD and Mooring Line Model for Floating Wind Turbine Hydrodynamics," In: *The 31st International Ocean and Polar Engineering Conference*. OnePetro.

Liu, Y, Li, S, Yi, Q, and Chen, D (2016). "Developments in Semi-Submersible Floating Foundations Supporting Wind Turbines: A Comprehensive Review," *Renewable and Sustainable Energy Reviews*, 60, 433-449.

Liu, Y, Xiao, Q, Incecik, A, and Peyrard, C (2019). "Aeroelastic Analysis of a Floating Offshore Wind Turbine in Platform-Induced Surge Motion Using a Fully Coupled CFD-MBD Method," *Wind Energy*, 22(1), 1-20.

Liu, Y, Xiao, Q, Incecik, A, Peyrard, C, and Wan, D (2017). "Establishing a Fully Coupled CFD Analysis Tool for Floating Offshore Wind Turbines," *Renewable Energy*, 112, 280-301.

Luan, C, Gao, Z, and Moan, T (2013). "Modelling and Analysis of a Semi-Submersible Wind Turbine with a Central Tower with Emphasis on the Brace System," In: *International Conference on Offshore Mechanics and Arctic Engineering*, 55423, V008T09A024.

Luan, C, Gao, Z, and Moan, T (2017). "Development and Verification of a Time-Domain Approach for Determining Forces and Moments in Structural Components of Floaters with an Application to Floating Wind Turbines," *Marine Structures*, 51, 87-109.

Koo, BJ, Goupee, AJ, Kimball, RW, and Lambrakos, KF (2014). "Model Tests for a Floating Wind Turbine on Three Different Floaters," *Journal of Offshore Mechanics and Arctic Engineering*, 136(2).

Masciola, M, Robertson, A, Jonkman, J, Coulling, A, and Goupee, A (2013). "Assessment of the Importance of Mooring Dynamics on the Global Response of the DeepCWind Floating Semisubmersible Offshore Wind Turbine," In: *Proceedings of the Twenty-third International Offshore and Polar Engineering Conference*, Anchorage, Alaska, USA.

Nygaard, TA, De Vaal, J, Pierella, F, Oggiano, L, and Stenbro, R (2016). "Development, Verification and Validation of 3DFloat; Aero-Servo-Hydro-Elastic Computations of Offshore Structures," *Energy Procedia*, 94, 425-433.

Palm, J, Eskilsson, C, Paredes, GM, and Bergdahl, L (2016). "Coupled Mooring Analysis for Floating Wave Energy Converters Using CFD: Formulation and Validation," In: *International Journal of Marine Energy*, 16, 83-99.

Palm, J, Moura Paredes, G, Eskilsson, C, Taveira Pinto, F, and Bergdahl, L (2013). "Simulation of Mooring Cable Dynamics Using a Discontinuous Galerkin Method," In: *5th International Conference on Computational Methods in Marine Engineering*, Hamburg, Germany, 455-466.

Robertson, A, Jonkman, J, Vorpahl, F, Popko, W, Qvist, J, Frøyd, L, Chen, X, Azcona, J, Uzunoglu, E, Guedes Soares, C, and Luan, C (2014). "Offshore Code Comparison Collaboration Continuation Within IEA Wind Task 30: Phase II Results Regarding a Floating Semisubmersible Wind System," In: *International Conference on Offshore Mechanics and Arctic Engineering*, 45547, V09BT09A012.

Robertson, AN, Wendt, F, Jonkman, JM, Popko, W, Dagher, H, Gueydon, S, Qvist, J, Vittori, F, Azcona, J, Uzunoglu, E, and Soares, CG (2017). "OC5 Project Phase II: Validation of Global Loads of the DeepCwind Floating Semisubmersible Wind Turbine," *Energy Procedia*, 137, 38-57.

Tran, TT, and Kim, DH (2015). "The Coupled Dynamic Response Computation for a Semi-Submersible Platform of Floating Offshore Wind Turbine," *Journal of Wind Engineering and Industrial Aerodynamics*, 147, 104-119.

Tran, TT, and Kim, DH (2016a). "A CFD Study into the Influence of Unsteady Aerodynamic Interference on Wind Turbine Surge Motion," *Renewable Energy*, 90, 204-228.

Tran, TT, and Kim, DH (2016b). "Fully Coupled Aero-Hydrodynamic Analysis of a Semi-Submersible FOWT Using a Dynamic Fluid Body Interaction Approach," *Renewable Energy*, 92, 244-261.

Yan, J, Korobenko, A, Deng, X, and Bazilevs, Y (2016). "Computational Free-Surface Fluid-Structure Interaction with Application to Floating Offshore Wind Turbines," *Computers and Fluids*, 141, 155-174.

Zhong W, Yim SC, and Deng L (2020a). "Vortex Shedding Patterns Past a Rectangular Cylinder Near a Free Surface," *Ocean Engineering*, 2020, 200, 107049.

Zhong W, Yim SC, and Deng L (2020b). "Reynolds-Number Effect on Flow Past a Rectangular Cylinder in the Presence of a Free Surface," *Ocean Engineering*, 2020, 216, 107865.

Zhou, Y, Xiao, Q, Liu, Y, Incecik, A, Peyrard, C, Li, S, and Pan, G (2019). "Numerical Modelling of Dynamic Responses of a Floating Offshore Wind Turbine Subject to Focused Waves," *Energies*, 12(18), 3482.